Modelling of near isothermal liquid piston gas compressor employing porous media for compressed air energy storage systems

Lee Haney[a], Robert Prosser[a], Alexander Lanzon[b], Yasser Mahmoudi[a,*]

[a] *The University of Manchester, Department of Mechanical and Aerospace Engineering, School of Engineering, Manchester, M13 9PL, UK*
[b] *The University of Manchester, Department of Electrical and Electronic Engineering, School of Engineering, Manchester, M13 9PL, UK*

Abstract

The liquid piston gas compressor (LPGC) is a method of compressing gases with improved efficiency. Key to the success of this device is its operation in as close to an isothermal state as possible. This paper presents high-fidelity, three-dimensional, unsteady Reynolds-averaged Navier-Stokes (uRANS) simulations to better understand the heat transfer and fluid physics involved in the liquid-piston-driven compression process. Furthermore, the uRANS is coupled with conjugate heat transfer to study using porous media inserts to manage the temperature increase. We simulate the entire cylinder/porous media arrangement using the volume of fluid (VOF) method to analyse the turbulent, multiphase physics and the fluid-structure interaction, providing a greater understanding of this process. It also investigates how porous media inserts perform against the no-insert (baseline) cases in producing a near-isothermal process. The porous mediums used are parallel plates, interrupted plates, and metal foam, all produced from aluminium. Results show that temperature rises within the cylinder can be reduced by as much as 120 K, depending on the choice of porous insert. This temperature reduction translates to an increase of up to 13% in compression efficiency.

Keywords: Computational Fluid Dynamics, Conjugate Heat Transfer, Liquid Piston Gas Compressor, Porous Media, Volume of Fluid

*Corresponding author
Email address: yasser.mahmoudilarimi@manchester.ac.uk (Yasser Mahmoudi)

Nomenclature

Symbols

A	Area	m^2
C	Constant	–
c	Specific heat	$\mathrm{J/kg \cdot K}$
Co	Courant number	–
g	Gravity	$\mathrm{m/s}^2$
H	Cylinder height	m
k	Turbulent kinetic energy	$\mathrm{m}^2/\mathrm{s}^2$
L	Porous media length	m
p	Pressure	bar
r	Radius	m
Re	Reynolds number	–
T	Temperature	K
t	Time	s
u	Fluid velocity	m/s
V	Volume	m^3
W	Work	J

Greek Symbols

α	Volume phase fraction	–
$\bar{\bar{\tau}}$	Stress tensor	$\mathrm{N/m}^2$

Δ	Difference	–
ϵ	Dissipation rate for kinetic energy	m^2/s^3
η	Compression efficiency	%
κ	Thermal conductivity	$W/m \cdot K$
μ	Dynamic viscosity	kg/ms
∇	Nabla	–
ρ	Density	kg/m^3
σ_k / σ_ϵ	Turbulent Prandtl number for k & ϵ, and Energy equation	–

Subscripts

0	Initial
a	Air
ave	Average
c	Compressed
f	Fluid
i	Inlet
in	Input
p	Pressure
s	Solid
s	Stored
t	Turbulent
w	Water

Acronyms

ACAES	Adiabatic compressed air energy storage
CAES	Compressed air energy storage
CFD	Computational fluid dynamics
CO_2	Carbon dioxide
DCAES	Diabatic compressed air energy storage
GW	Gigawatt
HTC	Heat transfer coefficient
LES	Large eddy simulation
LPGC	Liquid piston gas compressor
PISO	Pressure Implicit with Split Operators
PPI	Pores per inch
SA/V	Surface-area-to-volume
uRANS	Unsteady Reynolds-averaged Navier-Stokes
VOF	Volume of fluid

1. Introduction

The intermittent nature of renewable energy sources presents a significant challenge to electrical grid stability. Energy storage is a critical solution to this challenge, providing the flexibility to store surplus electricity when it is in demand. The majority of recent installations have been deployed as fast-response electricity storage, such as batteries. Currently, the UK operates with 1.6 GW of lithium battery storage, with another 1.5 GW under construction and a further 20 GW in development and planning stages [1]. Albeit mature, this type of technology is classed as a short-term storage method. Additional innovative, longer-term energy storage forms are required to ensure power supply security in all weather conditions (e.g., intermittency of renewable energy generation). Furthermore, this longer-term technology is essential to meet the planned 'Net Zero' emissions target of 2050 [2].

One approach that evades the issues associated with 'shorter-term' storage strategies is compressed air energy storage (CAES) systems [3]. CAES systems create electricity from the discharge of high-pressure air. Firstly, excess electricity from some external source is used to compress the working gas, which is then sent to the storage facility [4]. Before storage, thermal energy generated by the compression is lost, as the storage of 'hot air' is volumetrically inefficient. When power is required, the compressed air is discharged via an expander, which passes through an air turbine to generate the power [5]. The expanding air needs to be reheated by burning fossil fuels. This method has disadvantages due to the CO_2 emissions from burning natural gases in the high-pressure air before they flow into the turbine [4]. The existing plants that use this technology [4, 5] are classed as diabatic compressed air energy storage (DCAES) systems. Another CAES system has been conceived to reuse the heat created during the compression process. This concept is called adiabatic compressed air energy storage (ACAES).

ACAES systems are distinctive in using thermal energy storage (TES) units to capture the heat induced by air compression [6]. The stored thermal energy is transferred back to the expanding air when discharging. This propagation neutralises the adiabatic temperature drop and undertaking this cyclic heat transfer process mitigates the requirement for an auxiliary heat source. Advantages of this type of system are its long-duration electricity storage (days-weeks) combined with a medium-duration discharge (over 4 hours) while providing a high round-trip efficiency (RTE) [7].

One way to improve the efficiency of this ACAES system is to change

the compression and expansion method. The liquid piston gas compressor/expander (LPGC/E) is a combined compression and expansion unit (Figure 1) that uses a liquid to compress a working gas [8]. The first (compression) stage of the process is completed in the compression chamber before the high-pressure gas is dispatched to a repository. During the second (expansion) process, the recovered working fluid propels the liquid piston back down the chamber. The evacuated fluid passes through a pump and generator to produce electricity. The advantages of this method are that the liquid piston in this combined unit reduces gas leakages and is mechanically simple. The compressor/expander can be fitted with a porous medium inside the chamber to produce a near-isothermal compression/expansion cycle.

The key benefit of employing a liquid piston for compressing air is that the porous media in question can be used in the cylinder and reduce the peak air temperature, improving efficiency [9]. The porous media is usually a material with a high thermal conductivity. Porous media with complex geometries usually have a high surface-area-to-volume (SA/V) ratio and significantly greater heat transfer capabilities than simpler geometries. The additional increase in heat transfer is due to the complex shapes having shorter boundary layers [10]. These shorter boundaries break up the thermal boundary layer (as opposed to the long plates). The complex, varied geometries change flow angles, promoting mixing and increasing heat transfer [11]. The downfall with these geometries is that they usually come with higher pressure drops [12]. Open-cell metal foams have higher pressure drops than most porous media but are excellent at promoting mixing [13, 14].

Metal porous media inserts in compression and expansion is a proven method for increasing LPGC efficiency [15, 16]. At low pressures (10-12 bar), interrupted plates and open-cell aluminium foam have been seen to reduce the peak temperature by 90 to 120 K [17]. The baseline case was tested with an empty cylinder, and the efficiency was improved by filling the entire cylinder with porous media. Yan et al., [17] also achieved a reduction of between 57-75% of the baseline (no porous media) temperature, which leads to an 18% increase in compression efficiency.

Wieberdink et al., [15] assessed interrupted plates at pressures of up to 210 bar. At these higher pressures, the compression process reaches levels of 93% efficiency. Also, filling the top 13% of the LPGC with porous media at the higher pressure was as efficient in the lower-pressure case. The significant reason is the porous media engagement with the air and its duration. During compression, the air interacts with the porous media for the entire time

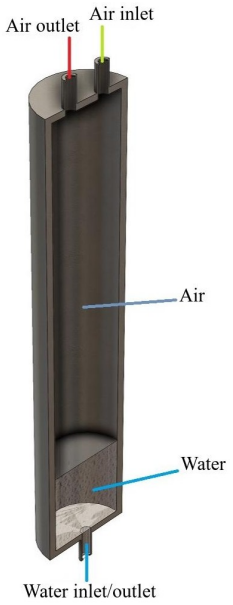

Figure 1: Illustration of liquid piston gas compressor/expander.

during both compression and expansion. Therefore, at its highest and lowest temperature points.

Patil et al., [16] investigate the use of different material porous media in the form of wire mesh. Aluminium and copper wire mesh spirals are fitted inside a compression chamber and tested at various flow rates. Via this method, the peak air temperature was reduced by up to 33 K, providing an efficiency improvement of up to 90%. Overall, this was an 8% improvement from the baseline cases. Khaljani et al., [9] used five aluminium parallel plates of various lengths to reduce the peak temperature. By partially filling the cylinder with five 0.5 m plates, the peak air temperature could be reduced by up to 80 K from the baseline case (450 K) during a 3.5-second compression stroke. Furthermore, this temperature reduction improves efficiency by 8% to 87% from the baseline case (79%). All these cases provide initial evidence that simple metal inserts effectively improve compression efficiency within an LPGC arrangement.

Multiple other approaches have been attempted to lessen the compressed air temperature and improve efficiency. Other methods such as micron-sized spray [18], aqueous foam [19], a high-speed fan [20] and cooling tubes [21] have been used in an attempt to counteract the temperature rise. Each

method has various successes and drawbacks in reducing final air temperature while improving the efficiency of the component.

Using a less complicated method, such as aluminium parallel plates, can reduce air temperature and improve efficiency by 16% and 8%, respectively [9]. Using more intricate geometrical features such as foam can reduce the air temperature by 80%, with an associated efficiency increase of 11% [22]. Applying more complicated methods, like aqueous foam [19] (efficiency $\approx$ 92%), high-speed fans [20] ($\approx$ 95%) and cooling tubes [21] ($\approx$ 99%), all claim to be effective in improving the overall efficiency of the component. However, they come with significant challenges when attempting to implement them at an operational level.

Given the relative parity of the differing approaches in terms of their performance, there is a case for using the simplest method to implement (i.e. a solid porous insert). Porous inserts reduce the system's complexity while maintaining a high-efficiency rate needed for a near-isothermal compression process. As a more direct method, the inserts reduce the need for maintenance due to the lack of moving parts compared with complex methods, such as aqueous foam and sprays. Although complex methods can be applied at a low-pressure range [23] with relative ease, they could become more challenging at higher pressure ranges/ratios and with larger volumes of air to cool. Also, controlling the spray systems could be challenging when scaling up the chamber size, as the studies performed are in small-scale chambers [18, 24]. Furthermore, a key aspect of using the liquid piston is to reduce the number of moving parts and simplify the system's complexity. Using these convoluted methods will only add to this problem. However, these complex cooling methods can enhance the compression efficiency [19]. Nevertheless, applying said methods will create more points of failure within a system than the porous inserts.

The existing research on the LPGC with porous inserts has been performed using simplified geometry of porous media (parallel plates) [9] or simplified methods of modelling complex porous media cases (metal foam) [25]. Methods such as representative elementary volume (REV) or the porous jump approach, which ignores the pore's intricate flow features, have been used to investigate such cases. This paper will investigate a pore-scale approach to the complex flow and thermal features of an LPGC employing porous inserts. It aims to shed light on the turbulent compressible and multiphase flow in the LPGC using porous media geometries of various complexities.

Table 1: Thermophysical properties of LPGC associated parts at $t = 0$.

Part	**Material**	$\boldsymbol{\rho}$ **(kg/m^3)**	$\boldsymbol{\kappa}$ **(W/m·K)**	$\boldsymbol{c_p}$ **(J/kg·K)**	$\boldsymbol{\mu}$ **(kg/m·s)**
Working gas	Air	1.205	0.03	1006	1.8×10^{-5}
Liquid Piston	Water	998	0.6	4187	8.9×10^{-4}
Cylinder	Stainless steel	8000	16	500	-
Porous Media	Aluminium	2719	237	871	-

2. Methodology

In this paper, computational fluid dynamic (CFD) simulations are conducted to establish how each porous media insert performs against the baseline case (no porous media) in the compression process. The liquid piston is water, and the working gas to be compressed is air. The porous media cases (Figure 2) examined are parallel plates, interrupted plates (linear and tilted) and a 'foam-like' lattice structure, all made from aluminium. The plates are spaced 5 mm apart in the transverse direction, and the interrupted plates have 5 mm gaps in the flow direction. The foam has pores of 5 mm in diameter, producing 20 pores per inch (PPI). The compression chamber is stainless steel with dimensions of 0.079 m diameter and 1 m length and a volume of 4.9l. The porous media inserts have an overall diameter of 0.077 m (giving 1 mm clearance between them and the chamber walls), and two section lengths are considered: 0.2 m and 0.4 m. The 0.2 m length insert is exposed solely to the airflow displaced by the liquid piston. The 0.4 m length insert is in contact with both air and water. Initially, the cylinder is filled with 10% (vol) of water and the remainder with air. Thermophysical properties for initial conditions ($t = 0$) can be found in Table 1.

2.1. Governing equations

The simulations investigate the complex features within the compressible, multiphase turbulent flow and use conjugate heat transfer to determine the heat transport in both fluid and solid phases. The turbulent flow is modelled using unsteady Reynolds-averaged Navier-Stokes (uRANS) equations. For

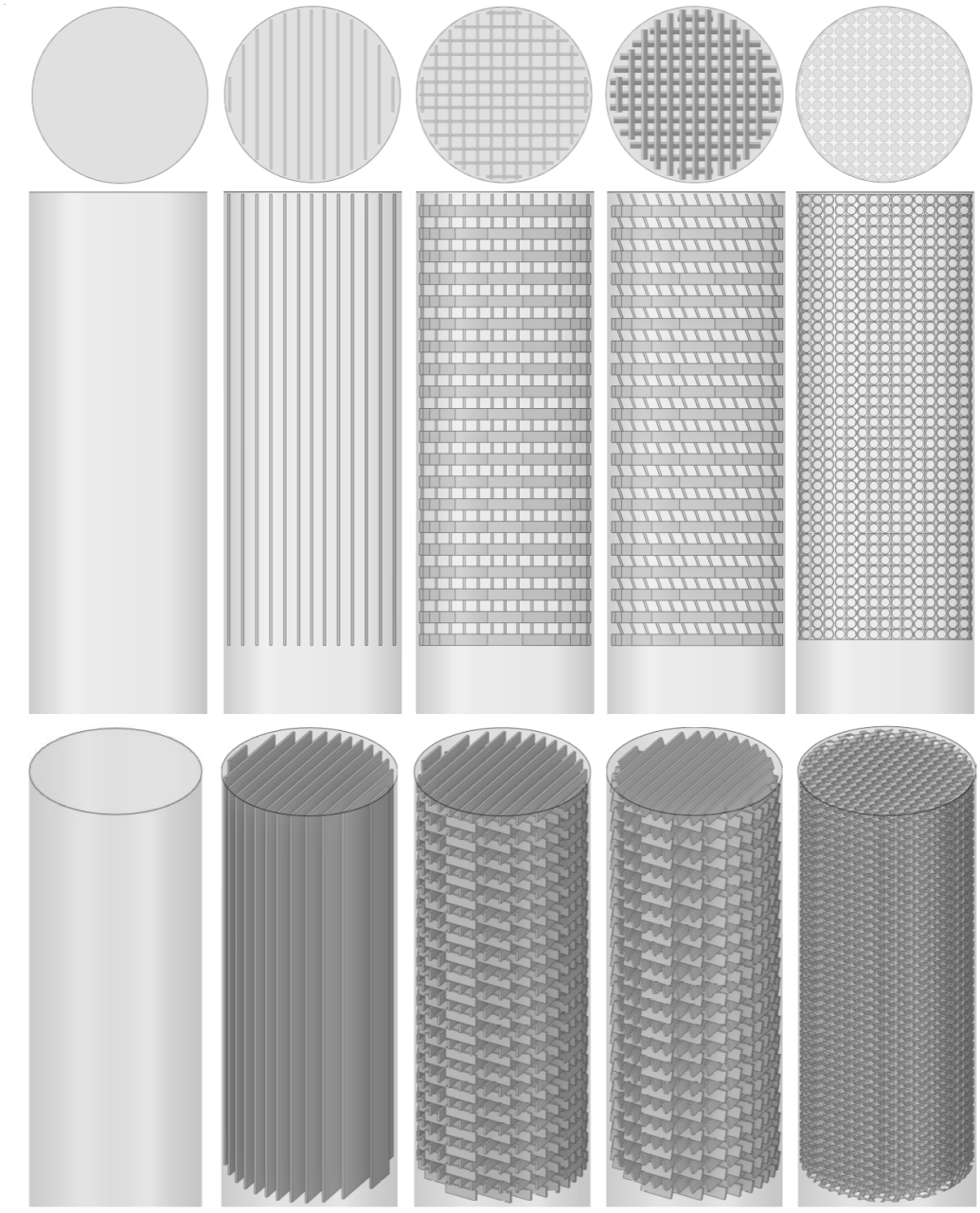

Figure 2: LPGC cases used for CFD simulations with plan, front and isometric views: (L-R) baseline (empty), parallel plates, interrupted plates - linear, interrupted plates - tilted, foam structure.

the multiphase problem, the volume of fluid (VOF) method can define the position of two immiscible fluids by tracking the volume fraction of both fluids and solving one set of equations. The Eulerian VOF method is applied in Ansys FLUENT [26] to track the interface between the water and air at each time step. By starting with the compressible continuity equation:

$$\frac{\partial \rho}{\partial t} + \nabla \cdot (\rho u) = 0, \tag{1}$$

we can modify this equation by applying functions of phase volume fraction, α, to numerically correspond to the transport of both fluid phases. Where air and water are shown as a and w, respectively. Therefore, the continuity equations for air is given by:

$$\frac{\partial \alpha_a \rho_a}{\partial t} + \nabla \cdot (\alpha_a \rho_a u) = 0. \tag{2}$$

Considering that the density is constant for water (incompressible fluid), therefore this can be translated into:

$$\frac{\partial \alpha_w}{\partial t} + \nabla \cdot (\alpha_w u) = 0. \tag{3}$$

Using the phase-averaged properties, the momentum equation is solved for both phases via:

$$\frac{\partial \rho u}{\partial t} + \nabla \cdot (\rho u u) = -\nabla p + \nabla \cdot \bar{\bar{\tau}} + \rho g, \tag{4}$$

where,

$$\rho = \alpha_a \rho_a + \alpha_w \rho_w, \tag{5}$$

and the stress tensor ($\bar{\bar{\tau}}$), which is based on the viscosity of the air-water mixture, is characterised as

$$\bar{\bar{\tau}} = 2\mu S, \tag{6}$$

and

$$\mu = \alpha_a \mu_a + \alpha_w \mu_w. \tag{7}$$

Also, using the mean-phase average properties, the energy equation for the fluid mixture is modelled as

$$\frac{\partial (\rho c_p T)}{\partial t} + \nabla \cdot (u(\rho c_p T + p)) = \nabla \cdot (\kappa_f \nabla T) \tag{8}$$

with,

$$\kappa_f = \alpha_a \kappa_a + \alpha_w \kappa_w, \tag{9}$$

$$\rho c_p = \alpha_a \rho_a c_{p,a} + \alpha_w \rho_w c_{p,w}. \tag{10}$$

For the porous media (solid inserts), the energy equation is combined with the fluid phase as

$$\frac{\partial}{\partial t}(\rho c_s T) = \nabla \cdot (\kappa_s \nabla T). \tag{11}$$

The standard $k - \epsilon$ solver is employed for the turbulent flow within the cylinder. For the turbulent kinetic energy (k) and its rate of dissipation (ϵ), the following equations are employed:

$$\frac{\partial(\rho k)}{\partial t} + \nabla \cdot (\rho k u) = \nabla \cdot \left[\left(\mu + \frac{\mu_t}{\sigma_k} \right) \nabla k \right] + P_k - \rho \epsilon, \tag{12}$$

$$\frac{\partial(\rho \epsilon)}{\partial t} + \nabla \cdot (\rho \epsilon u) = \nabla \cdot \left[\left(\mu + \frac{\mu_t}{\sigma_\epsilon} \right) \nabla \epsilon \right] + \frac{C_{\epsilon_1} \epsilon}{k} P_k - C_{\epsilon_2} \rho \frac{\epsilon^2}{k}. \tag{13}$$

The shear production of turbulence (P_k) is defined as,

$$P_k = \mu_t S^2, \tag{14}$$

with S as the modulus of mean rate-of-strain tensor,

$$S \equiv \sqrt{2 S_{ij} S_{ij}}. \tag{15}$$

Furthermore, the turbulent viscosity (μ_t) is determined by the following

$$\mu_t = \rho C_\mu \frac{k^2}{\epsilon}. \tag{16}$$

The Prandtl numbers for k and ϵ are given as σ_k and σ_ϵ, respectively, and the turbulent model constants are $C_{\epsilon 1}$ and $C_{\epsilon 2}$. These constant parameters are [26]:

$$\sigma_k = 1.00 \quad \sigma_\epsilon = 1.30 \quad C_\mu = 0.09 \quad C_{\epsilon 1} = 1.44 \quad C_{\epsilon 2} = 1.92$$

2.2. Compression efficiency

Improving the heat transfer so a near-isothermal process is achieved during the compression will make the process more efficient [15, 16]. Two variables govern how close the process is to being isothermal: these are the input work (W_{in}) and the energy stored (E_s). The input work is given as the work to compress the initial volume of air at ambient conditions (P_0, V_0) to its final, compressed pressure and volume (P_c, V_c). This is defined by either the $P-V$ or $T-V$ profile. The input work can be expressed as [17]:

$$W_{in} = (P_c - P_0)V_c - \int_{V_0}^{V_c} (P - P_0)\, dV, \tag{17}$$

E_s is the quantity of work extracted from the compressed air as it is expanded to its initial conditions. If the expansion is slow enough, it occurs as an isothermal process. If the expansion is fast, an adiabatic process will take place. In assuming an isothermal expansion, this method quantifies the highest potential energy of the reserved cool gas. The storage energy is expressed as:

$$E_s = P_0 V_0 \ln \left| \frac{P_c}{P_0} \right|, \tag{18}$$

where P_c/P_0 is the compression ratio. The compression efficiency is the ratio of the energy storage to the work input,

$$\eta_c = \frac{E_s}{W_{in}}. \tag{19}$$

2.3. Boundary conditions

An inlet velocity of 0.1785 m/s is used for all simulations leading to a compression time of up to 3.5 seconds, depending on pressure drop created by the porous media. The initial pressure and temperature are set to 2.5 bar and 298 K, respectively. Wall boundary conditions are set for the cylinder with the adiabatic and no-slip conditions applied. The porous media thermal settings are applied through conjugate heat transfer within the solver [26]. The air is treated as an ideal gas under compression since pressures are low (10 bar) temperature differences are relatively small (450 K). The initial fluid settings are given in Table 1, all values are fixed bar density, which will vary over the course of the compression. The values are fixed to alleviate some of the computational cost. For example, dynamic viscosity changes

are a function of temperature, by applying Sutherland's law [27] over the temperature range the change in viscosity would be in the range of $2 \times 10^{-6} < \mu < 7 \times 10^{-6}$ kg/m·s. Therefore, this viscosity change and potential effects can be regarding as negligible. Furthermore, the initial surface tension is set at 0.072 mN and the initial contact angle for the interface is 90 degrees.

2.4. Simulation parameters

First-order implicit methods are used for the transient formulation, and a second-order upwind scheme is used for the spatial derivatives. The PISO (Pressure Implicit with Splitting Operators) algorithm is applied for pressure-velocity coupling. The least squares cell-based method is used to calculate the gradients of variables. All simulations use a time step of 1×10^{-4} seconds, giving a Courant number condition of $Co < 1$. The Courant number ($Co = \frac{u_i \Delta t}{\partial x}$) in this case needed to be less than one due to the transient aspect of the simulations.

2.5. Computational meshing

The domain is divided into sections with different mesh densities, with finer mesh placed around the inserts and coarser meshing towards the bottom of the cylinder. Depending on the complexity of the inserts, the mesh cell count ranges between 6 million to 30 million elements. As the geometry inside the cylinder becomes more intricate, more elements are required to resolve the flow and thermal boundary layers for these geometries. A y_+ value of less than five is imposed around the critical areas of interest for all simulations.

2.6. Mesh independence study

During the initial stages, domain geometry and grid layout are fundamental concerns in obtaining a successful simulation solution. A mesh independence study is performed for all simulations to ensure the results are independent of the mesh resolution. The baseline case (Figure 3a and b) and one porous media case (Figure 3c and d) will be reviewed in this study. Mesh independence is conducted on all cylinder/heat exchanger combinations. However, only the $h = 0.2$ parallel plate case is shown for the porous media cases to avoid repetition. All values are taken throughout the centreline of the cylinder. The X-axis plots the dimensionless height within the cylinder (Y/H), 0 being the inlet and 1 being the top wall of the cylinder.

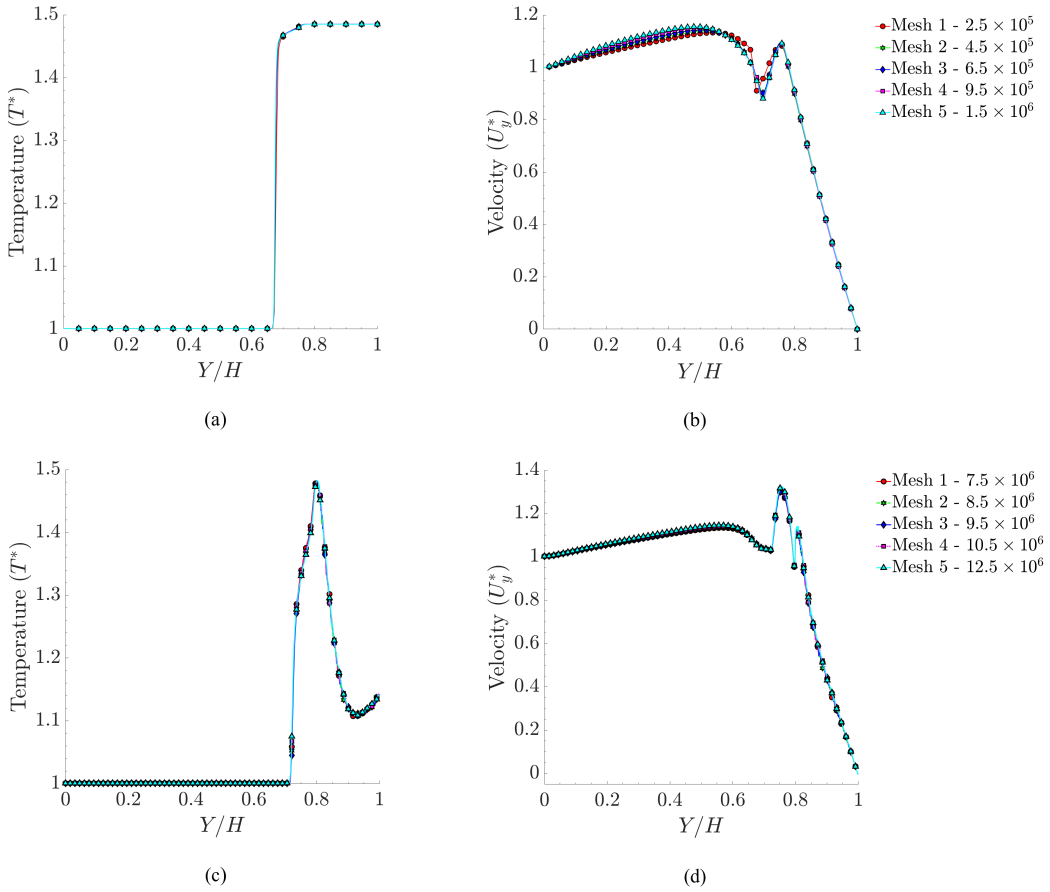

Figure 3: Mesh independence study in which (a) dimensionless temperature (T^*) and (b) velocity (U_y^*) are plotted for the baseline cases. For the porous media case, (c) dimensionless temperature and (d) velocity are plotted. Five meshes are used which increase in refinement from mesh 1 to 5.

Table 2: Dimensionless (normalised) values.

Parameter	**Normalised value**
Pressure (P)	$P^* = P/P_0$
Velocity ($U_{x,y,z}$)	$U^*_{\varnothing} = U_{\varnothing}/U_0$
Temperature (T)	$T^* = T/T_0$
Turbulent kinetic energy (k)	k/U_i^2
Density (ρ)	$\rho^* = \rho/\rho_0$
Porous media length (L)	$h = L/H$
X-coordinates (X)	X/r
Y-coordinate (Y)	Y/H
Z-coordinate (Z)	Z/r

Overall, mesh results do not vary much between all cases. Comparisons between the fine (mesh 4 and 5) and the medium (mesh 3) resolution meshes show that the values do not deviate drastically. There are slight variation between the coarse and fine meshes in both baseline and porous media cases. However, in both studies the deviations between mesh 3 and mesh 5 can be classed as negligible so that the changes can be disregarded, especially when the accuracy difference is minimal. The trade off is a reduction in the element count of over nine hundred thousand for the baseline; and, 3.2 million for the parallel plate case. Therefore, no additional refinement is needed as mesh 3 can be demonstrated to be sufficiently accurate for both cases.

2.7. Dimensionless variables

Dimensionless (normalised) values will be used to compare parameters with other studies using different liquid piston arrangements. Table 2 displays the variables, the scaling factor, and the normalised parameter used throughout.

2.8. Validation

Experimental data from previous studies [9, 15, 17, 28] are used as a comparison to validate the current numerical results. Experiments were conducted on empty cylinders comparable to the baseline case in this study. Figure 4 displays the pressure/temperature-volume charts, which are normalised (Table 2) for ease of comparison. The pressure (P^*) values observed in all cases follow a similar path in the initial stages, only to vary later due to the different compression ratios. The present CFD case does not vary much

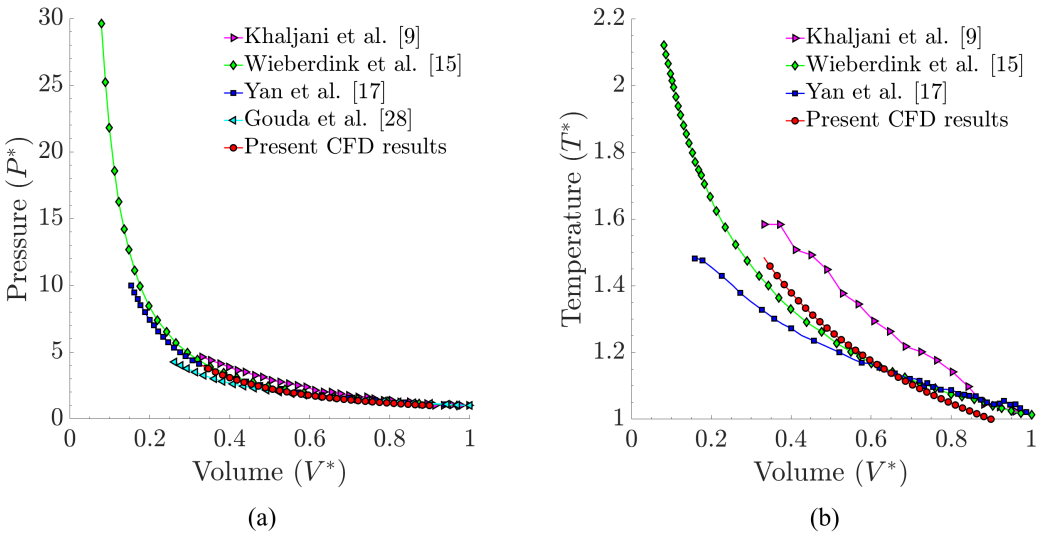

Figure 4: (a) Normalised P-V and (b) T-V comparisons between the current baseline simulation case against various experimental works from Khaljani et al. [9], Wieberdink et al. [15], Yan et al. [17] and Gouda et al. [28].

from all the experimental works but is most comparable to the Yan et al.' [17] study regarding P-V progression.

Furthermore, the final T^* values of the numerical results are that of the Yan study. Also, the Khaljani [9] follows a similar path to the numerical results. The differences between the Khaljani case can be attributed to a slight difference in the geometry and experimental variables. The cylinder height ($h = 0.1$) and compression ratio (four to five) increase in their experimental [9] study. Changes in said variables can be attributed to the deviation in temperature developments throughout all studies. During these baseline compression cases, there is approximately a 6.6% difference between the numerical and experimental [9] final temperature values. Given this slight variation, the numerical model accurately predicts the pressure and temperature increase in this liquid piston arrangement.

3. Results

This section presents a detailed analysis of the numerical results, with comparisons made to results from the Neu and Subrenat [29] study, which analyses the flow fields during a baseline compression process. The results

are split into baseline (no porous media) and porous media cases. The baseline cases provide insight into the temperature rise and the flow physics. The porous media cases explore the effects of turbulence on enhancing heat transfer. The results for the baseline case are shown over the compression process duration. The porous media cases are given at the end of the compression cycle (10 bar absolute).

3.1. Baseline case (no porous media)

Baseline cases were performed to set benchmarks for the final air temperature at the end of the compression cycle and to see how the gas behaves during compression. Figure 5a shows that at the end of the compression process. The average air temperature (T^*_{ave}) of 1.48 (440 K) is reached with a compression time of approximately 3.19 seconds providing the worst-case temperature rise. The mitigation of which is sought via porous media. With this in mind, this empty cylinder case has a compression efficiency of 81.7%. At the onset of the compression process, boundary layer formation is absent at the walls above the water-air interface. Yet, as the compression process advances, the boundary layer undergoes a significant evolution, forming a distinctive funnel-like feature. Despite the use of a fixed inlet velocity (U^*), this asymmetric feature results in a 20% increase in velocity above the water-air interface and along the centreline in the Y-axis (Figure 5b). Which was followed by a progressive reduction in air velocity in the rest of the domain.

This effect is further displayed through the radial velocity (U^*_x) above the water-air interface, where these velocities continue to increase as the compression progresses (Figure 5c). This recirculation is initially caused by forced convection as the hot air is compressed, and the cooler cylinder wall evolves into a complex interplay of adverse velocities. Compared to the experimental data, the results align during the initial phases. During the early stages of Neu and Subrenat's [29] work, the flow structure is close to that of our numerical work. With zero velocity at the wall and the gradient increasing to the centreline. Furthermore, the opposing radial velocities across the cylinder are similar with ± 0.2 m/s values, which can be seen in both numerical and experimental work.

The key difference between this numerical study and the experiment work [29] is capturing how the flow transitions from laminar into a more turbulent regime. Our results do not exhibit these turbulent features due to the model's limitations. The standard k-epsilon model calculates the mean flow characteristics via a time-averaging method, which can provide lower fidelity

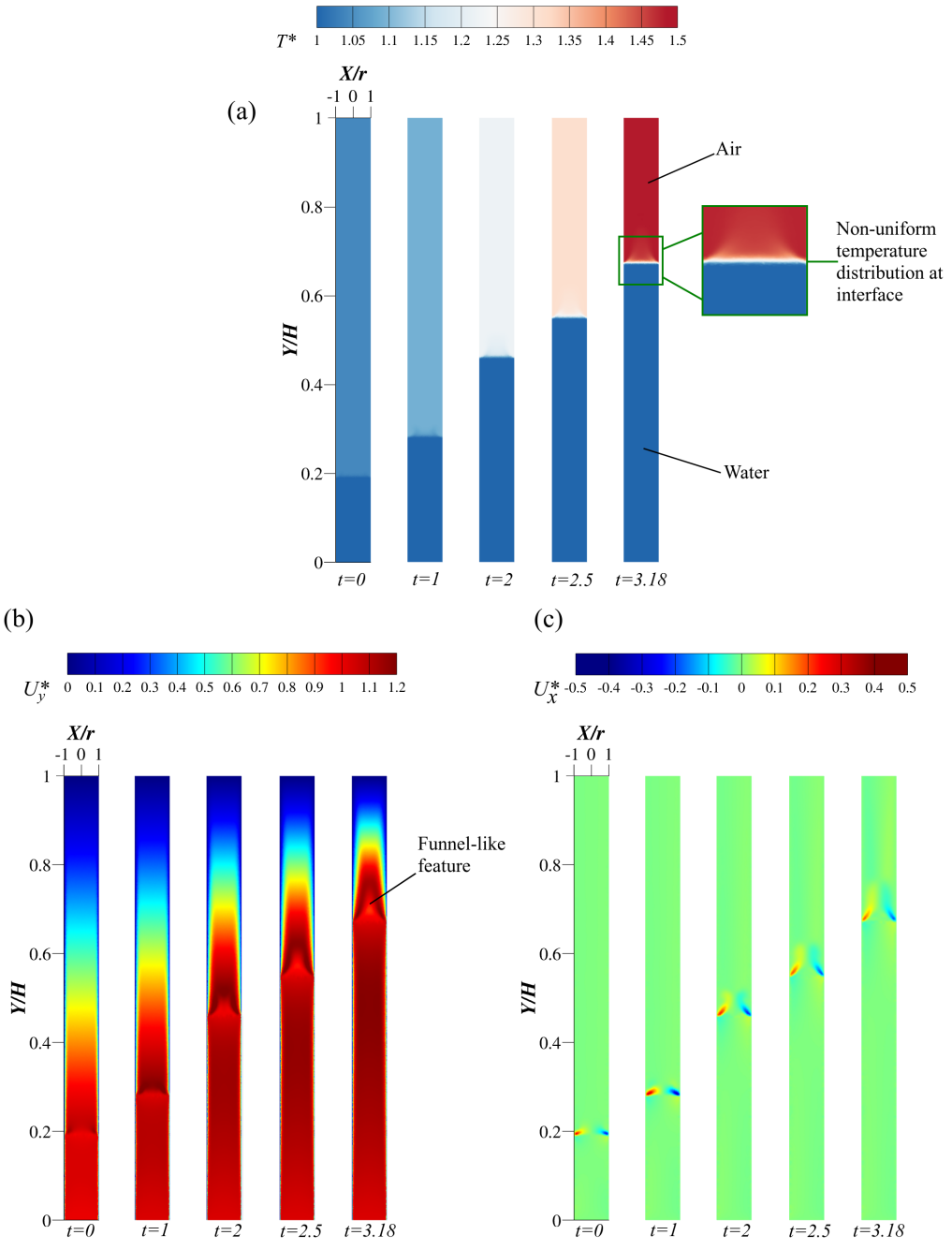

Figure 5: Contours from (a) dimensionless temperature (T^*), (b) dimensionless axial velocity (U_y^*) and (c) dimensionless radial velocity (U_x^*) at different time-steps throughout the compression process.

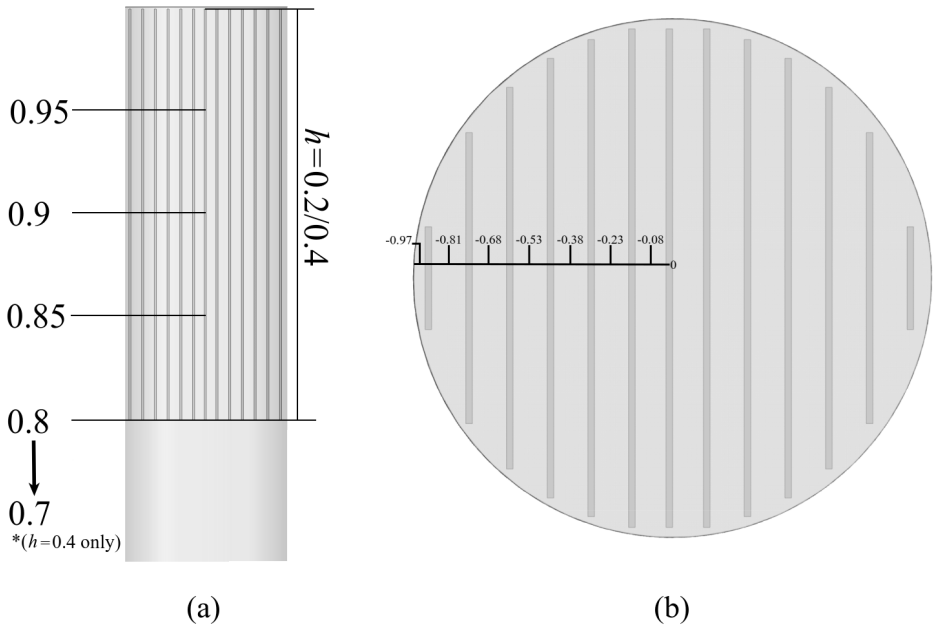

Figure 6: Data extraction locations for (a) Y/H and (b) X/r locations in porous media cases.

results when dealing with complicated flow structures. However, higher fidelity techniques such as large eddy simulation (LES) modelling have been used [30, 31] in baseline cases and simple conjugate heat transfer models (cylinder walls only). LES can capture the intricate flow features with a higher degree of accuracy by resolving the larger-scale eddies. Also, it provides more accurate results by accounting for the instantaneous (fluctuating) flow variables compared to the time-averaged method. However, uRANS was chosen for this study due to its ability to handle the complexity of adding porous media without significantly increasing computational costs.

3.2. Porous media cases

Porous media inserts are essential in producing a near-isothermal process by increasing the heat transfer between itself and the working gas [15, 17]. Accomplishing this can reduce the final air temperature by increasing the available heat transfer surface area, improving compression efficiency. In this paper, we change the arrangement of the porous media to significantly expand the SA/V ratio, thereby enhancing the heat transfer capabilities within the system (Table 3). For example, changing the porous media configuration

Table 3: Porous media surface area and volumes.

LPGC cases	**SA [m^2]**	**V [m^3]**	**SA/V Ratio**
Baseline (no porous media)	-	-	-
Parallel plates: $h = 0.2$	0.304	1.48×10^{-4}	2045:1
Interrupted plates - linear: $h = 0.2$	0.352	1.48×10^{-4}	2371:1
Interrupted plates - tilted: $h = 0.2$	0.367	1.48×10^{-4}	2498:1
Metal foam: $h = 0.2$	0.323	1.03×10^{-4}	3130:1
Parallel plates: $h = 0.4$	0.606	2.97×10^{-4}	2040:1

from parallel plates to interrupted plates or open-cell metal foam further increases the surface area, thus improving the heat transfer between the air and the porous media. However, this improvement comes at the cost of increased geometric complexity and higher manufacturing costs, particularly when transitioning from parallel plates to metal foam.

Another parameter tested is the porous media length. The effects of the insert length were analysed for the parallel plate case using lengths of $h = L/H = 0.2$ and $h = 0.4$. Placing plates with a length of $h = 0.2$ inside the compression chamber allows the porous media to interact with the air exclusively. This allows for a higher volume of air to be compressed. By extending the plate length to $h = 0.4$, the elements become partly submerged in the water, which will reduce the further temperature by cooling the plates.

Also, Wieberdink et al., [15] found that filling only the top half of the cylinder (air section) provides similar efficiency to cases where the porous media extends the entire cylinder length. Compared to the full-length configuration, partially filling the chamber offers several advantages. Partial filling allows more air to occupy the chamber, enabling the compression of a larger volume of air per stroke. A shorter porous media design decreases material costs while contributing to a lighter overall system. For these reasons, this study opted for inserts that filled only the top air section of the cylinder.

Furthermore, turbulence levels are analysed within the porous media. By simulating a whole porous media arrangement rather than REV, turbulence is investigated without using some form of average values to calculate the Reynolds (Re) number. Using a normalised turbulent kinetic energy (k/U_i^2), we can visualise how localised flow disturbances caused by the porous media

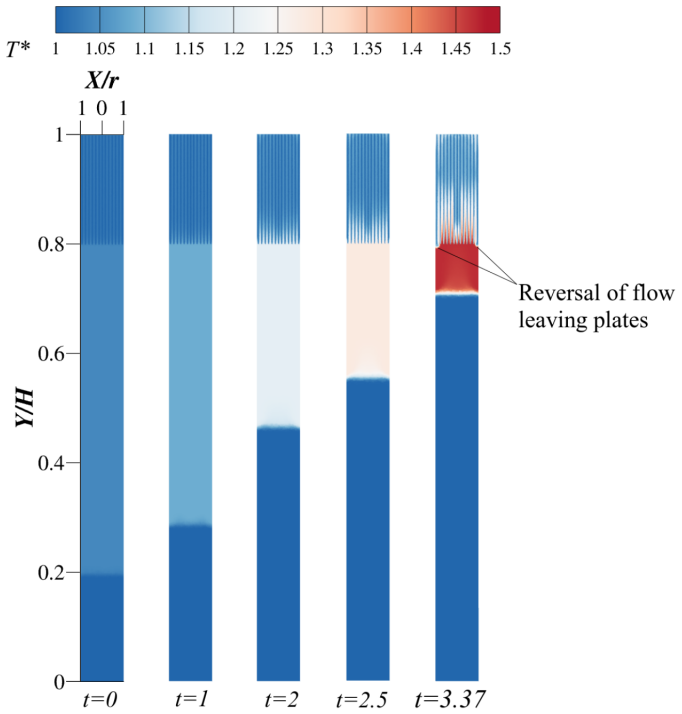

Figure 7: T^* distribution for the parallel plate case at a length of $h = 0.2$ during different time-steps throughout the compression process. Time of 3.37 seconds corresponds to the end of the compression process.

affect the heat transfer. For our results, data is taken at Y/H positions, which span the cylinder's diameter. Furthermore, the X/r data positions are taken at a radial point and through the length of the porous media inserts (Figure 6).

3.2.1. Parallel plate cases at lengths $h = 0.2$ and $h = 0.4$

In this case, by placing parallel plates in the cylinder, the final air T^*_{ave} is restricted to around 1.12 (332.75 K) from the initial value of 1 (298 K). The compression process takes approximately 3.36 seconds with a pressure drop ($\Delta P/h$) of approximately 95.8 Pa/m. Added friction from the porous media inserts creates this differential in pressure. During compression, this reduction in the air temperature is observed the higher the air travels vertically through the porous media inserts. Figure 7 shows that this temperature reduction is distributed non-uniformly within the plates. This ranges from 1.33 (396 K) from the base to 1.15 (342 K) at the top of the cylinder, giving

the air a 0.18 (54 K) variation across the plates. The average plate T^* rise is just over its initial value of 1.

During this, the higher heat transfer coefficient (HTC) values occur at the stagnation region at the plate entrance. This value gradually decreases, moving towards the trailing edge of the porous media. With a slight increase is observed at the top of the plates. This increase in heat transfer is localised in the areas of higher levels of turbulence (Figures 9b and 10a). At the cylinder wall, the boundary layer above the water-air interface grows. Adding the plates creates a further differential as the air enters and travels up these thin channels. A channelling effect occurs when the air enters the porous media and U_y^* increases significantly. Turbulent kinetic energy levels are boosted as U_y^* increases. When the boundary layer approaches $X/r = 0$ on both sides, the velocity sees a 20% reduction from the initial value when entering the plates.

However, figures 7 and 8 show that the temperature reduction decreases as the velocities increase. The elongated feature of these plates will create an extended thermal boundary layer (Figure 9) over the length of the plates. Convective heat transfer is restricted due to the thickness of this thermal boundary layer. Also, a negative U_y^* value between the cylinder wall and the neighbouring plate is observed as the reversed flow leaves the porous media. Along with the recirculation, a further narrowing between the final plate and wall and the added convection causes this reversal. To sustain the turbulence seen at the plate entrance, the geometry must be optimised to maintain these levels while reducing the thermal boundary layer.

Results for the parallel plates of $h = 0.2$ are similar to Khaljani et al.' [9] experimental study regarding temperature reduction. They use five plates of the same length to achieve a T^* reduction of 0.16 (50 K). Compared to the thirteen in this case, which reduces the air temperature by 0.36 (107.49 K). A 2.4 times plate increase leads to a 2.15 times reduction in air temperature. Increasing the plate quantity displays the interrelationship between expanding the surface area and transferring heat in the LPGC. Also, widening the plate widths will affect turbulence production within the plates.

Extending the porous media length inside the cylinder is another promising avenue for enhancing overall heat transfer. This approach substantially improves heat transfer by many factors. Firstly, the insert surface area is increased for heat transfer. Doubling the area increases the HTC (section interacting only with air) to 246.83 W/m^{2}K—an improvement of 59% from the $h = 0.2$ case. Secondly, submerging the plates in water plays a significant

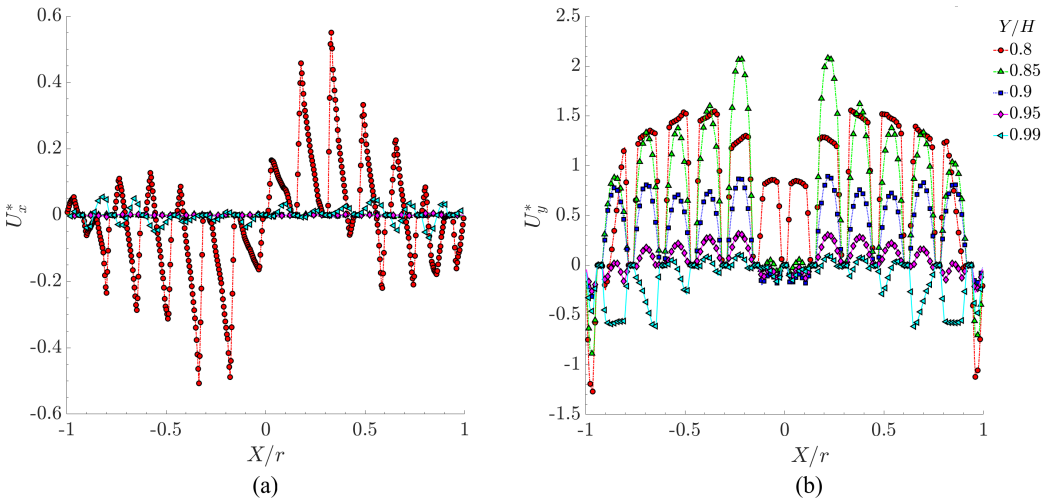

Figure 8: (a) U_y^* and (b) U_y^* velocity components in the in parallel plate case at length of $h = 0.2$ at different Y/H positions.

role in improving efficiency. The water reverses the heat flux in the bottom section of the plates, adding a cooling effect. Nevertheless, the pressure drop trade-off arises again as this increases to 3354.9 Pa/m. The presence of water within the extended inserts requires further work to overcome this loss due to the added viscosity. Even though this pressure drop figure increases from the shorter inserts, a compression time of 3.42 seconds is achieved.

From a turbulence production perspective, the submergence is a negative. Figure 12 displays how immersion of the insert significantly diminishes turbulent effects. Even though U_y^* increases by 50% due to the channelling effects from the narrow gaps, U_x^* and turbulent kinetic energy are greatly reduced. Still, the temperature increase is significantly suppressed due to the emphasis on increased SA/V ratio and negative heat flux. A reduction to the overall T_{ave}^* temperature is just above 1.07 (320 K). Figure 11 demonstrates a uniformity in the temperature distribution throughout, with a slight temperature increase of near 1.25 (372 K) in the regions with increased turbulence (Figures 11b and 12c). Also, the air is contained within the porous media due to the plates being submerged. This development eliminates all the higher-temperature air from the $h = 0.2$ cases between the water-air interface and the plate entrance.

Furthermore, the efficiency of the parallel plates with a $h = 0.4$ is the highest at over 93%. Increasing approximately 6% from the $h = 0.2$ plates

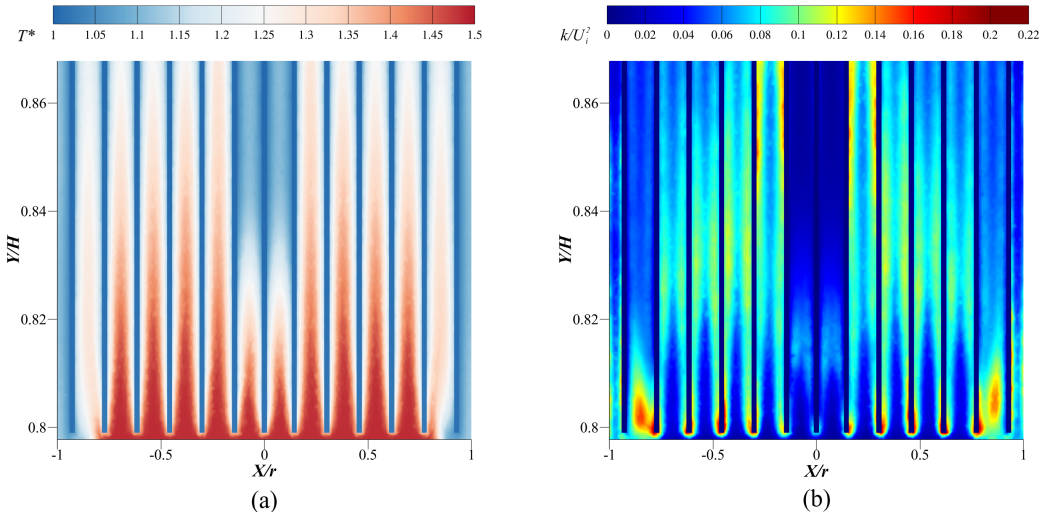

Figure 9: (a) Normalised temperature (T^*) and (b) turbulent kinetic energy $\left(k/U_i^2\right)$ distribution in parallel plate entrance in length of $h = 0.2$. Both variables displaying the formation of secondary boundary layer over the plates.

and over 12% from the baseline case. The subsequent sections will examine the effects of the modified porous media geometries on the compression process.

3.2.2. Interrupted plates (linear and tilted) cases at the length $h = 0.2$

Refining the geometry by decreasing the lengths and stacking the plates expands the surface area by 14.76% (parallel plates: $h = 0.2$). The geometries do not vary volumetrically but altering the profile of the porous media creates better heat transfer attributes from parallel to interrupted plates. Thus, increasing the SA/V ratio further improves the heat transfer abilities of the inserts. Altering the geometry breaks up the thermal boundary layer. Regardless, compression time is slightly increased to 3.39 seconds with an increased pressure drop of 103.67 Pa/m. Although the linear interrupted plates still produce a channel flow, this structure also promotes mixing by splitting up the viscous sub-layer of flow with the shorter plates. Analogous to the parallel plates, the temperature reduction is non-uniform. Still, this porous media type exhibits significantly less high-temperature air towards the base and less temperature variability inside than the parallel plates of $h = 0.2$. Figure 13 shows that by changing the arrangement of the plates and using interrupted plates in different arrangements, T^*_{ave} can be further

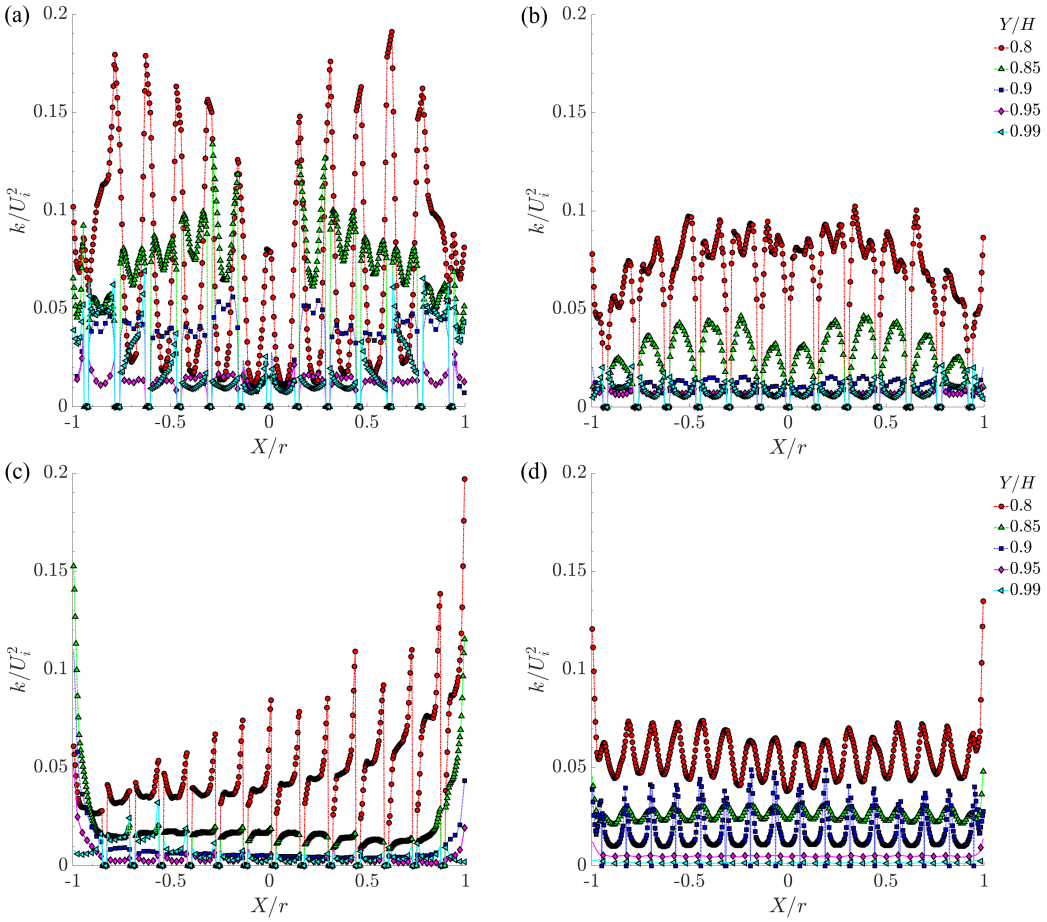

Figure 10: Non-dimensional turbulent kinetic energy $\left(k/U_i^2\right)$ values for all porous media types at $h = 0.2$. Figures are taken end of compression cycle (approximately 3.4 seconds). Porous media type: (a) parallel plates, (b) linear interrupted plates, (c) tilted interrupted plates, (d) foam structure.

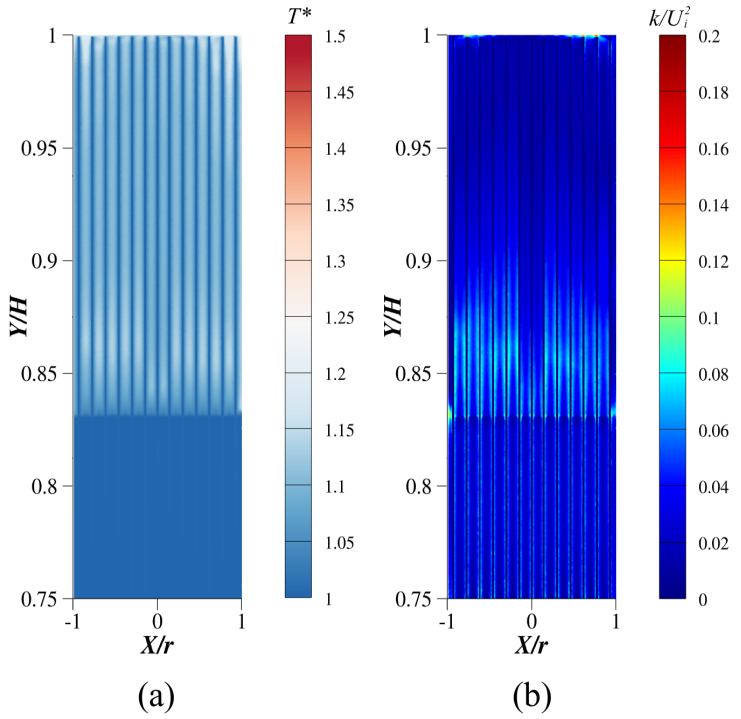

Figure 11: (a) Temperature (T^*) and (b) turbulent kinetic energy $\left(k/U_i^2\right)$ distribution in parallel plate case at length of $h = 0.4$. Figures taken end of the compression process (3.42 seconds).

reduced to around 1.1 (326.64 K).

As the flow passes through the channels, it mixes freely in each subsection. The production of vortices can be seen in each longitudinal section (Figure 14), where the density difference across the plates is at its highest. From the entrance of the cylinder, ρ^* increases from around 6.5 to 9.5 between 0.9-0.95 Y/H mark, which is approximately a 46% increase. This originates from the temperature disparity between fluid and solid. Also, viscous/form drag comes into effect from the plates, which can also be characterised as between Darcy and Forchheimer-type flows ($\approx 10 < Re < 150$). Stated flows border on laminar to unsteady laminar; this is evident in Figure 10b in which turbulence levels are non-existent between these Y/H values.

Furthermore, tilting the plates should increase heat transfer capabilities theoretically; this is due to the expanded SA/V ratio (5.6% increase). The tilt angle was selected following the Zhang [32] study. Zhang found that tilting the angle of the plates between 0 and 40 degrees increases the heat

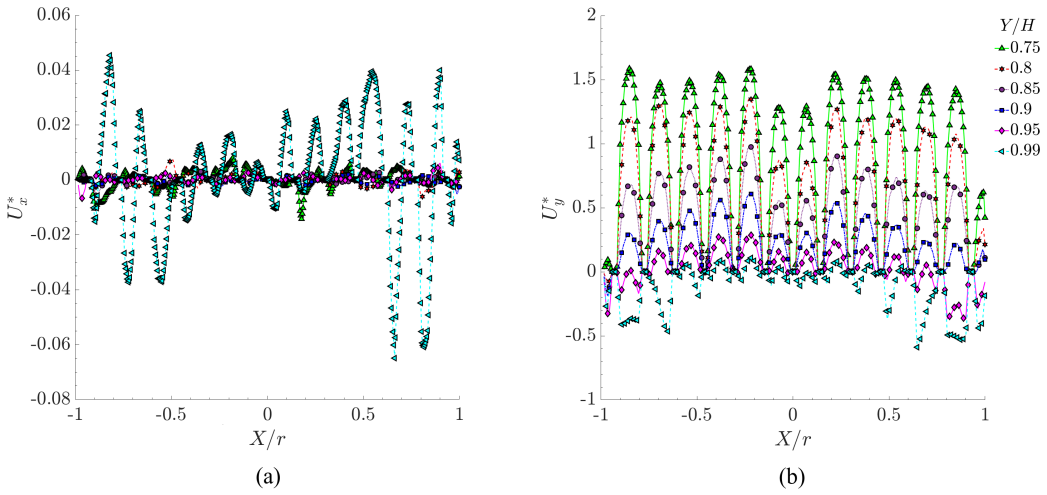

Figure 12: (a) U_x^* and (b) U_y^* velocity components at different Y/H positions of parallel plate case at length of $h = 0.4$. Figures taken at end of compression cycle (3.42 seconds).

transfer. The increased impingement on the plates leads to a progressively intricate pore-scale fluid flow. This geometric change increases turbulence and, therefore, heat transfer. Therefore, a median angle of 20 degrees in the X- and Z-axes (Figure 2) was selected for this study. However, Zhang's [32] study only implemented REV methods for simulating this type of setup, in which the full effects of this plate arrangement are not observed.

The flow is forced into the direction of the tilt, as this is 20° from left to right, creating a spiralling effect through the porous media. Evident in the U_x^* and U_y^* velocity profiles in Figure 15. After the initial entry to the tilted plate, as per the linear plates, the heat transfer becomes more uniform throughout both porous media. Figure 13 illustrates that even with these added heat transfer enhancements, the temperature distribution through both sets of interrupted plates is nearly identical. In both cases, the ΔT between the air T_{ave}^* and the plate temperature are negligible. Again, with a higher surface area, frictional forces increase to raise the pressure drop to 109.5 Pa/m. Leading to a compression time of 3.43 seconds.

Figure 10c displays close to a three-to-four times increase in turbulence kinetic energy in the tilted plates in localised areas that follow the tilt direction. This increase is also observed in the U_y^* velocity profile, and the HTC peaks at around 1360.79 W/m^{2}K. Although there are fluctuations in localised areas, the tilt reduces the overall turbulence levels throughout the insert. If

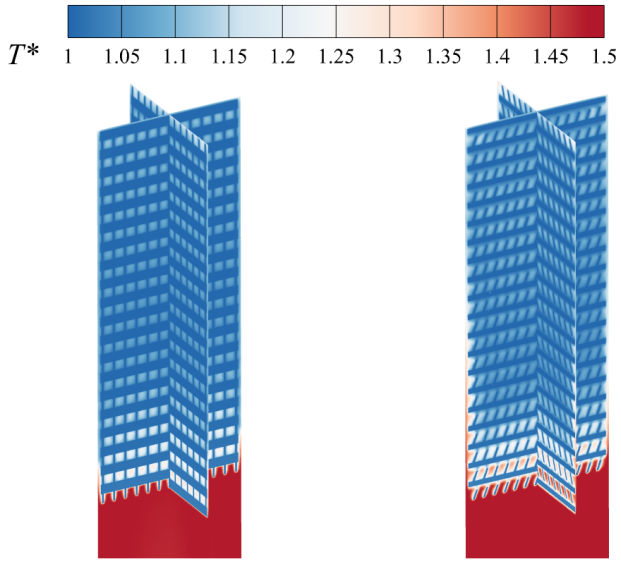

Figure 13: T^* distribution for the (a) interrupted and (b) tilted plate cases at a length of $h = 0.2$.

the tilted geometry and varying angles can be optimised to improve overall turbulence levels, this could be a promising avenue regarding heat transfer in this application. Furthermore, creating a swirling flow can increase heat transfer by fifty percent compared to the non-swirling flow with identical inlet conditions [33]. In this case, the overall HTC of the tilted plates increases by approximately 11.8% (22 W/m^{2}K) over its linear interrupted counterpart (173.25 W/m^{2}K). Still, this added heat transfer efficiency only improves by 0.45% between the linear (87.95%) and tilted (88.4%) versions.

3.2.3. Metal foam case at a length of $h = 0.2$

Lastly, this geometry modification changes the structure to one that is not linear in its features as per the other inserts. A "foam-like" lattice structure was created to enhance the SA/V ratio and turbulence further. The foam holds the highest SA/V ratio of 3130:1. It averages a HTC of 265.21 W/m^{2}K, the highest of all the porous media cases. The HTC increase is due to higher heat flux and a reduction in ΔT between the insert and air. It is further acknowledging the importance of this variable in heat transfer. Turbulent kinetic energy and HTC levels are highest through the initial plate

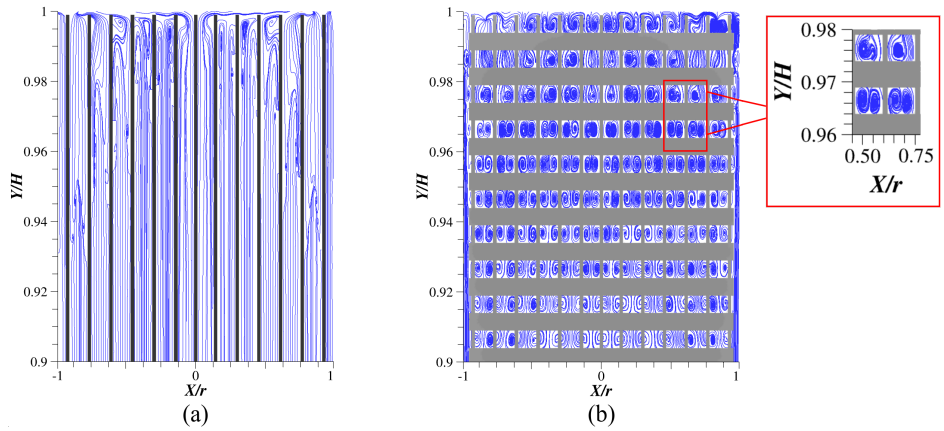

Figure 14: Streamlines within top 10% section of the (a) parallel plate and (b) linear interrupted plate cases at a length of $h = 0.2$.

entrance. Turbulence remains steady until around the $Y/H = 0.85$ mark (Figure 10d). The increase in turbulence and velocity is a direct result of the increased surface area and the pores across the bottom face of the insert. Figure 16 shows an U_y^* increase to approximately 1.6 as it passes through the plate/pore entrance, U_x^* velocity exhibits high values again at this point only. As the air passes through with this increased velocity through the pores, the temperature reduction is minimal.

Figure 17 displays that as the air enters the insert at a T^* of slightly less than 1.5, it is drastically cooled and is reduced to slightly over one towards the top of the cylinder. The overall T_{ave}^* reduces to approximately 1.1 (328.19 K). The higher the porous media the air travels, the more all these values (T^*, U^*) are reduced significantly. As per the interrupted plates, the air temperature distribution is more uniform than the parallel plates. An average temperature increase of 0.101 (30.1 K) from the initial baseline cases is further evidence for a near-isothermal process using this porous media type.

However, compression time rises to 3.48 seconds with a further pressure drop of 113.29 Pa/m. This pressure drop might not be significant during a fast flow rate case, as the compression only rises 0.28 seconds from the baseline case, therefore not requiring significant extra work. Once coupled with a longer compression time, the effects of this pressure drop may become detrimental to the amount of work needed to compress the air. Nevertheless, changing the structure to a foam lattice shape improves efficiency up

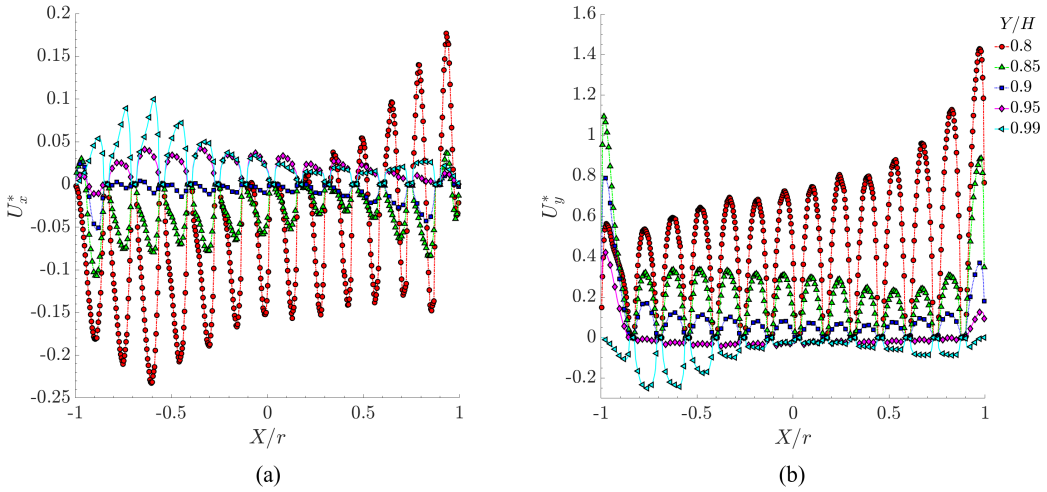

Figure 15: (a) U_x^* and (b) U_y^* velocity profiles for the tilted plate case of $h = 0.2$.

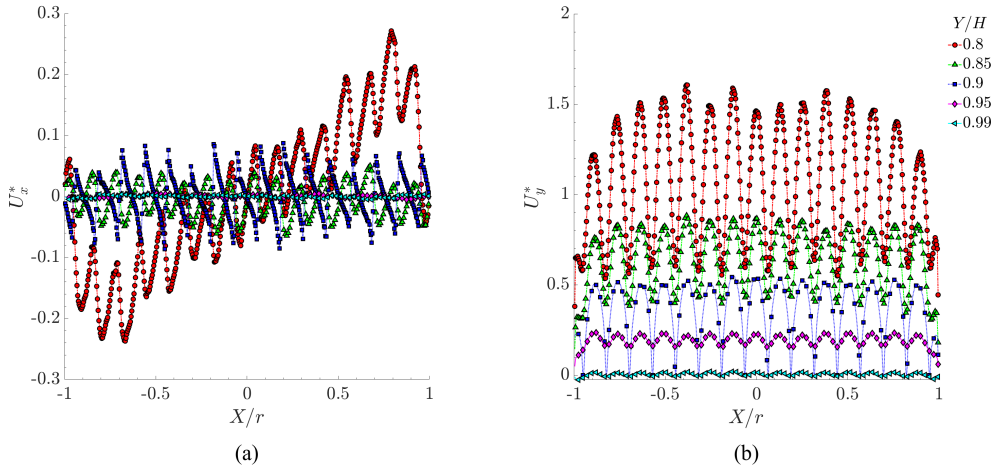

Figure 16: (a) U_x^* and (b) U_y^* velocity components at different Y/H positions in the metal foam case of $h = 0.2$.

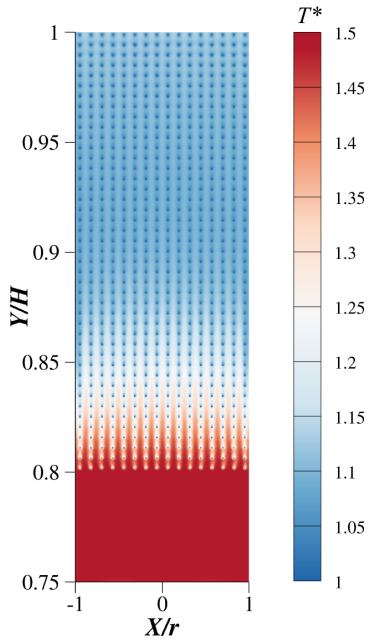

Figure 17: T^* distribution at end of compression process in the metal foam case of $h = 0.2$.

to approximately 89%. However, this is only a 1% difference from the linear interrupted plates. The lattice structure is still relatively structured compared to metal foams from other studies. Future work is needed to optimise the porous media to increase turbulence through stochastic methods [34] to improve the HTC. Therefore, it is an additional enhancement to the compression process. Regarding thermal management, the trade-off between porosity and pore size is the crucial aspect [13]. Nevertheless, with a value of approximately 89%, this is a good starting point to improve these structures.

4. Conclusion

A compressible, multiphase, turbulent heat transfer analysis was performed to investigate the heat transfer and fluid flow within a Liquid Piston Gas Compressor. The LPGC compresses air at ambient temperature from 2.5 to 10 bar. The primary focus of this study was to increase the heat transfer within the cylinder by using porous media inserts. Four different types (at two lengths) of porous inserts were used. Geometric changes to the insert were made to evaluate various parameters such as the SA/V ratio, turbulence properties and the effect of water cooling. The increased heat

transfer with the porous media for the compression process reduces the final air temperature to as near isothermal as possible. Therefore, this increase in SA/V ratio and turbulence enhancement improves the overall compression efficiency. Further geometry optimisation is needed to take full advantage of turbulence production within the inserts rather than just elevated levels at the entrance.

Coupling the extended length with more intricate geometries can increase compression efficiency, but a significant trade-off is required for these more extended inserts. With a performance improvement, there is a reduction in the volume of air to be compressed. On a relatively small-scale component such as this five-litre unit, is the extra 4% performance worth the loss in compressed air. Nevertheless, the pressure drop produced by the extended inserts creates another limitation to overcome.

Further preliminary investigations are ongoing concerning how reduced flow rates and compression time can affect the heat transfer within the porous media. The current results take up to 3.5 seconds to complete a compression cycle. Slowing this process gives the porous media more time to interact with the air. Furthermore, this work will investigate how both fluids interact with the plates and if any turbulence is featured within the complex geometries. Extending the complex geometries to this length will further reduce overall air temperature. Further breaking up the thermal boundary layer to allow for more mixing will enhance the heat transfer abilities. Also, following the trend in Table 3, the SA/V ratio will increase, further enhancing efficiency. It is essential to note that the issue with these longer porous media is the increased mesh sizes, which will be more computationally expensive than the $h = 0.2$ cases.

Furthermore, future work will be undertaken on how both compression and expansion processes using porous media will affect the round-trip efficiency (RTE) if implemented in an ACAES system. Said work would be comparable to the Gouda et al.' [35] study in which the RTE of a baseline case is investigated. Employing a similar approach but applying the methodology from this study or a higher fidelity model will provide greater insight into the LPGC/E effectiveness if implemented into an ACAES system.

Declaration of competing interest

The authors declare that they have no known competing financial interests or personal relationships that could have appeared to influence the work

reported in this paper.

Acknowledgements

This work was supported by the UK Engineering and Physical Sciences Research Council (EPSRC) [grant numbers EP/Y017471/1]. The authors would like to acknowledge the assistance given by Research IT and the use of the Computational Shared Facility at The University of Manchester.

References

[1] National Grid, Pathways to 2050 - National Grid ESO publishes 2019 Future Energy Scenarios, 2019. URL: https://www.nationalgrideso.com/document/273166/download.

[2] GOV.uk, UK Becomes First Major Economy to Pass Net Zero Emissions Law, 2019. URL: https://www.gov.uk/government/news/uk-becomes-first-major-economy-to-pass-net-zero-emissions-law.

[3] S. D. Garvey, A. J. Pimm, Compressed air energy storage (caes), Storing Energy (Second Edition) with Special Reference to Renewable Energy Sources (2022) 117–140. doi:10.1016/b978-0-12-824510-1.00031-3.

[4] D. R. Hounslow, W. Grindley, R. M. Loughlin, J. Daly, The development of a combustion system for a 110 mw caes plant, Journal of Engineering for Gas Turbines and Power 120 (1998) 875–883. doi:10.1115/1.2818482.

[5] F. Crotogino, K. U. Mohmeyer, R. Scharf, Huntorf caes: More than 20 years of successful operation, 2001.

[6] B. Cárdenas, S. Garvey, A directly charged thermal store for compressed air energy storage systems, Journal of Energy Storage 71 (2023) 108183–108183. doi:10.1016/j.est.2023.108183.

[7] M. Khaljani, J. Harrison, D. Surplus, A. Murphy, P. Sapin, C. Markides, Y. Mahmoudi, A combined experimental and modelling investigation of an overground compressed-air energy storage system with a reversible liquid-piston gas compressor/expander, Energy Conversion and Management 245 (2021) 114536. doi:10.1016/j.enconman.2021.114536.

[8] J. D. Van de Ven, P. Y. Li, Liquid piston gas compression, Applied Energy 86 (2009) 2183–2191. doi:10.1016/j.apenergy.2008.12.001.

[9] M. Khaljani, A. Vennard, J. Harrison, D. Surplus, A. Murphy, Y. Mahmoudi, Experimental and modelling analysis of efficiency enhancement in a liquid piston gas compressor using metal plate inserts for compressed air energy storage application, Journal of Energy Storage 42 (2021) 103240. doi:10.1016/j.est.2021.103240.

[10] Y.-L. He, W.-Q. Tao, Convective heat transfer enhancement: Mechanisms, techniques, and performance evaluation, Advances in Heat Transfer 46 (2014) 87–186. doi:10.1016/bs.aiht.2014.09.001.

[11] M. Jadidi, H. K. Param, A. Revell, Y. Mahmoudi, Large eddy simulations of turbulent heat transfer in packed bed energy storage systems, Journal of Energy Storage 59 (2023) 106449. doi:10.1016/j.est.2022.106449.

[12] K. Nilpueng, L. G. Asirvatham, A. S. Dalkılıç, O. Mahian, H. S. Ahn, S. Wongwises, Heat transfer and fluid flow characteristics in a plate heat exchanger filled with copper foam, Heat and Mass Transfer 56 (2020) 3261–3271. doi:10.1007/s00231-020-02921-x.

[13] S. Mancin, C. Zilio, A. Cavallini, L. Rossetto, Pressure drop during air flow in aluminum foams, International Journal of Heat and Mass Transfer 53 (2010) 3121–3130. doi:10.1016/j.ijheatmasstransfer.2010.03.015.

[14] D. Y. Kim, K. C. Kim, An experimental study on the thermal and hydraulic characteristics of open-cell nickel and copper foams for compact heat exchangers, International Journal of Heat and Mass Transfer 130 (2019) 162–174. doi:10.1016/j.ijheatmasstransfer.2018.10.084.

[15] J. Wieberdink, P. Y. Li, T. W. Simon, J. D. Van de Ven, Effects of porous media insert on the efficiency and power density of a high pressure (210 bar) liquid piston air compressor/expander – an experimental study, Applied Energy 212 (2018) 1025–1037. doi:10.1016/j.apenergy.2017.12.093.

[16] V. C. Patil, J. Liu, P. I. Ro, Efficiency improvement of liquid piston compressor using metal wire mesh for near-isothermal compressed air

energy storage application, Journal of Energy Storage 28 (2020) 101226. doi:10.1016/j.est.2020.101226.

[17] B. Yan, J. Wieberdink, F. Shirazi, P. Y. Li, T. W. Simon, J. D. Van de Ven, Experimental study of heat transfer enhancement in a liquid piston compressor/expander using porous media inserts, Applied Energy 154 (2015) 40–50. doi:10.1016/j.apenergy.2015.04.106.

[18] J. Guanwei, X. Weiqing, C. Maolin, S. Yan, Micron-sized water spray-cooled quasi-isothermal compression for compressed air energy storage, Experimental Thermal and Fluid Science 96 (2018) 470–481. doi:10.1016/j.expthermflusci.2018.03.032.

[19] V. C. Patil, P. I. Ro, Experimental study of heat transfer enhancement in liquid piston compressor using aqueous foam, Applied Thermal Engineering 164 (2020) https://doi.org/10.1007/s11242–019–01357–014441. doi:10.1016/j.applthermaleng.2019.114441.

[20] M. Specklin, M. Deligant, P. Sapin, M. Solis, M. Wagner, C. N. Markides, F. Bakir, Numerical study of a liquid-piston compressor system for hydrogen applications, Applied Thermal Engineering 216 (2022) 118946. doi:10.1016/j.applthermaleng.2022.118946.

[21] N. Cerkovnik, V. Costa, A. Lopes, Modeling and parametric optimization of a liquid piston compressor with inner cooling tubes, Applied Thermal Engineering 228 (2023) 120436–120436. doi:10.1016/j.applthermaleng.2023.120436.

[22] X. Weiqing, D. Ziyue, W. Xiaoshuang, C. Maolin, J. Guanwei, S. Yan, Isothermal piston gas compression for compressed air energy storage, International Journal of Heat and Mass Transfer 155 (2020) 119779. doi:10.1016/j.ijheatmasstransfer.2020.119779.

[23] G. Jia, X. Nian, W. Xu, Y. Shi, M. Cai, Water-spray-cooled quasi-isothermal compression method: Water-spray flow improvement, Entropy 23 (2021) 724. doi:10.3390/e23060724.

[24] B. Ahn, V. C. Patil, P. I. Ro, Effect of integrating metal wire mesh with spray injection for liquid piston gas compression, Energies 14 (2021) 3723. doi:10.3390/en14133723.

[25] C. Zhang, J. H. Wieberdink, F. A. Shirazi, B. Yan, T. W. Simon, P. Y. Li, Numerical investigation of metal-foam filled liquid piston compressor using a two-energy equation formulation based on experimentally validated models, Volume 8B: Heat Transfer and Thermal Engineering (2013). doi:10.1115/imece2013-63854.

[26] Ansys, Ansys Fluent Theory Guide, 2022. URL: https://ansyshelp.ansys.com/account/secured?returnurl=/Views/Secured/corp/v201/en/flu_th/flu_th.html?q=ansys%20fluent%20theory%20guide.

[27] W. Sutherland, Lii. the viscosity of gases and molecular force, The London, Edinburgh, and Dublin Philosophical Magazine and Journal of Science 36 (1893) 507–531. doi:10.1080/14786449308620508.

[28] E. M. Gouda, Investigation of a compressed air energy storage system: Flow and heat transfer numerical modeling in a liquid piston, Ph.D. thesis, Nantes Université, 2021.

[29] T. Neu, A. Subrenat, Experimental investigation of internal air flow during slow piston compression into isothermal compressed air energy storage, Journal of Energy Storage 38 (2021) 102532. doi:10.1016/j.est.2021.102532.

[30] E. M. Gouda, M. Benaouicha, T. Neu, Y. Fan, L. Luo, Flow and heat transfer characteristics of air compression in a liquid piston for compressed air energy storage, Energy 246 (2022) 124305. doi:10.1016/j.energy.2022.124305.

[31] T. D. Nguyen, J. Rendall, S. Kowalski, Numerical study of liquid piston compression using large-eddy simulation and volume-of-fluid approach, OSTI OAI (U.S. Department of Energy Office of Scientific and Technical Information) (2023). doi:10.1115/imece2023-110906.

[32] C. Zhang, CFD Simulations and Thermal Design for Application to Compressed Air Energy Storage, Ph.D. thesis, University of Minnesota, 2015.

[33] M. A. Pakhomov, The effect of flow swirling on flow structure, turbulence and heat transfer in turbulent droplet-laden flow in a pipe sudden

expansion, Journal of Physics: Conference Series 1105 (2018) 012052. doi:10.1088/1742-6596/1105/1/012052.

[34] W. Alruwaili, M. Jadidi, A. Keshmiri, Y. Mahmoudi, Pore-scale conjugate heat transfer analysis of turbulent flow over stochastic open-cell metal foams, International Journal of Thermal Sciences 202 (2024) 109061–109061. doi:10.1016/j.ijthermalsci.2024.109061.

[35] E. M. Gouda, T. Neu, M. Benaouicha, Y. Fan, A. Subrenat, L. Luo, Experimental and numerical investigation on the flow and heat transfer behaviors during a compression–cooling–expansion cycle using a liquid piston for compressed air energy storage, Energy 277 (2023) 127622–127622. doi:10.1016/j.energy.2023.127622.